Molecular bond stabilization in the strong-field dissociation of O_2^+

P. M. Abanador,[1] T. Pauly,[2] and U. Thumm[1]
[1]*J. R. Macdonald Laboratory, Department of Physics, Kansas State University, Manhattan, Kansas 66506, USA*
[2]*Department of Physics and Astronomy, Drake University, Des Moines, Iowa 50311, USA*

(Received 24 January 2020; accepted 24 March 2020; published 20 April 2020)

We theoretically examine the rotational and vibrational dynamics of O_2^+ molecular ions exposed to intense, short laser pulses for conditions realized in contemporary pump-probe experiments. We solve the time-dependent Schrödinger equation within the Born-Oppenheimer approximation for an initial distribution of randomly aligned molecular ions. For fixed peak intensities, our numerical results show that total, angle-integrated $O_2^+ \to O(^3P) + O^+(^4S^0)$ dissociation yields do not monotonically increase with increasing infrared-probe pulse duration. We find this pulse-duration-dependent stabilization to be consistent with the transient trapping of nuclear probability density in a light-induced (bond-hardening) potential-energy surface and robust against rotational excitation. We analyze this stabilization effect and its underlying bond-hardening mechanism (i) in the time domain, by following the evolution of partial nuclear probability densities associated with the dipole-coupled $O_2^+(a\ ^4\Pi_u)$ and $O_2^+(f\ ^4\Pi_g)$ cationic states, and (ii) in the frequency domain, by examining rovibrational quantum-beat spectra for the evolution of the partial nuclear probability densities associated with these states. Our analysis reveals the characteristic timescale for the bond-hardening mechanism in O_2^+ and explains the onset of bond stabilization for sufficiently long pulse durations.

DOI: 10.1103/PhysRevA.101.043410

I. INTRODUCTION

The ionization of gaseous molecules in intense short pulses of light typically results in the transient coherent excitation of electronically, vibrationally, and rotationally excited molecular cations. In many cases, the intramolecular nuclear dynamics in the excited molecular ions can be described in terms of nuclear wave packets that are generated by ionization of the parent molecule and represented as coherent superpositions of rovibrational stationary states in several adiabatic Born-Oppenheimer (BO) electronic states of the external-field-free molecular ion (see, e.g., Refs. [1–5] and refs. therein).

The excited initial vibrational-states distribution in the molecular ion is usually modeled in the Franck-Condon (FC) approximation assuming instantaneous ionization, i.e., based on the nuclear wave-function overlap between the ground state of the neutral parent molecule and excited vibrational states in the relevant adiabatic electronic states of the molecular ion [2,6]. The FC approximation often provides reasonable estimates of the excited vibrational-states amplitudes and was successfully applied in many dissociative-ionization (DI) calculations that compare favorably with experimental data, even though it does not yield relative initial phases of the excited stationary rovibrational-state constituents of the nuclear wave packet. It thus leaves the shape of the initial cationic nuclear wave packet undetermined [7,8]. Cationic vibrational-state distributions calculated in FC approximation tend to be vibrationally warmer than those obtained by modeling the initial ionization process based on molecular Ammosov-Delone-Krainov (ADK) tunneling-ionization rates [3,6].

After its creation by ionization of the neutral molecule, the nuclear motion of the molecular ion for any given initial rotational state is determined by the coherent evolution of nuclear rovibrational wave packets on adiabatic ionic potential energy surfaces [9–12]. This coherent expansion into adiabatic BO electronic states of the molecular ion is justified by the three orders of magnitude difference between the timescales of the fast intramolecular electronic and slow nuclear motion. In numerical solutions of the time-dependent Schrödinger equation (TDSE) this expansion is typically truncated in BO approximation to only include the few lowest adiabatic BO states. The BO approximation is routinely applied in intense-light–molecule interaction calculations and validated in many applications by favorable agreement with measured photoelectron emission and fragment-kinetic-energy release (KER) data.

In the absence of stochastic external forces that compromise the coherence of the nuclear wave packet during the time the nuclear motion is tracked (typically tens of femtoseconds for studies of the vibrational motion in molecular hydrogen, hundreds of femtoseconds for the vibrational motion in heavy diatomic molecules, and several picoseconds if the combined rovibrational motion is of interest), the distribution of rovibrational states remains coherent. It changes due to (i) nonadiabatic couplings near conical intersections (spatial regions of degenerate or nearly degenerate adiabatic potential energies of the molecular ion) and (ii) light-induced couplings near resonant transitions between electronic states. Due to different energy eigenvalues, the rovibrational stationary-state components of the excited cationic wave packet evolve with different phase accumulations [9–13]. This leads to a continuously changing shape and localization of the nuclear wave packet. Such cycles of dephasing and reviving localized nuclear wave packets have been observed in measured KER spectra resulting from the laser-induced dissociation of diatomic molecules

[1,7,14] and agree with nuclear wave-packet calculations performed within the FC and BO approximations [1,14–16].

Starting with pioneering pump-probe experiments in the 1980s [17], the evolution and ultimate fate of light-excited molecular cations has been probed experimentally and modeled theoretically in a large number of studies. In many of these investigations, the molecular dynamics initiated by excitation and ionization in an ultrashort pump pulse is destructively imaged by dissociating the excited diatomic molecular cation in delayed ultrashort probe pulses [1,4,8,14,15,18,19]. Scanning the pump-probe delay over a sufficiently large delay range while recording KER spectra for each delay allows the time-resolved mapping of the bound motion and dissociation pathways in excited molecules. After initial applications of this technique recorded the nuclear motion in relatively heavy molecules with a time resolution of picoseconds [20], ultrafast laser technology rapidly evolved to allow the mapping of the faster vibrational motion in lighter molecular cations with femtosecond time resolution, impressively demonstrating, e.g., the quantum nature of the nuclear motion in terms of alternating sequences of nuclear wave-packet dephasing and revivals [13] in pump-probe-delay dependent fragment KER spectra [2,7,14,15,21,22].

Owing to their comparatively simple structure, diatomic molecules have been comprehensively investigated in pump-probe studies. Among those, neutral hydrogen molecules and hydrogen molecular cations have the most simple structure and have thus become widely studied prototypical systems (for a recent review see Ref. [23]). Despite their simplicity they display a wide range of molecular strong-field effects that are often (yet not always) amenable to fairly accurate numerical simulations. In fact, phenomena such as the above mentioned nuclear wave packet revivals [2,7,15], charge-resonance enhanced ionization [24–26], and bond softening and bond hardening [2,19,27–29] were first investigated for hydrogen molecules. The prominence of hydrogen molecular ions for time-resolved pump-probe studies of their excited nuclear dynamics extends to the development of computational and analytical techniques. Examples for these techniques are, respectively, the representation of the external-field-dressed molecular structure in terms of adiabatic BO-Floquet molecular potential surfaces [2,28,30] and the quantum-beat analysis in the frequency domain of time-resolved fragment KER spectra [1,3,6,11,12,14,15,19] which we apply in this work.

The interaction between molecules and laser electric fields can lead to the formation of potential wells along specific nuclear coordinates (for diatomic molecules along the internuclear distance R) [2,28,30]. As an example, Fig. 1 shows the field-induced one-photon avoided crossing between the Floquet potential curves associated with the field-free $a\,^4\Pi_u$ and $f\,^4\Pi_g$ electronic states of $O_2{}^+$. This avoided crossing is located at the intersection of the field-free $O_2{}^+(a\,^4\Pi_u)$ BO potential curve and the field-free $O_2{}^+(f\,^4\Pi_g)$ curve downshifted by the photon energy ω. The upper field-dressed (Floquet) potential curve features a well that tends to trap nuclear probability density. Over the past three decades, the transient existence of such "bond-hardening" potential wells has triggered questions about the significance of vibrational trapping for the dissociation dynamics and, in particular, whether bond hardening is observable as a pulse-intensity (or energy) dependent stabilization against molecular dissociation [2,19,27–29]. Vibrational trapping is possible when part of the nuclear vibrational wave packet overlaps a vibrational bond hardening well. While the Floquet picture provides an intuitive description of the strong-field dissociation process, two main mechanisms—bond hardening and bond softening—compete in determining the final, measurable dissociation yield. In the interpretation of molecular-dissociation experiments, it is therefore difficult to isolate the effects of each of these mechanisms. Whether vibrational trapping occurs, how it can possibly be revealed in pump-probe experiments, and the extent to which it impedes dissociation for a given molecule and set of pump- and probe-pulse parameters are intriguing unanswered questions.

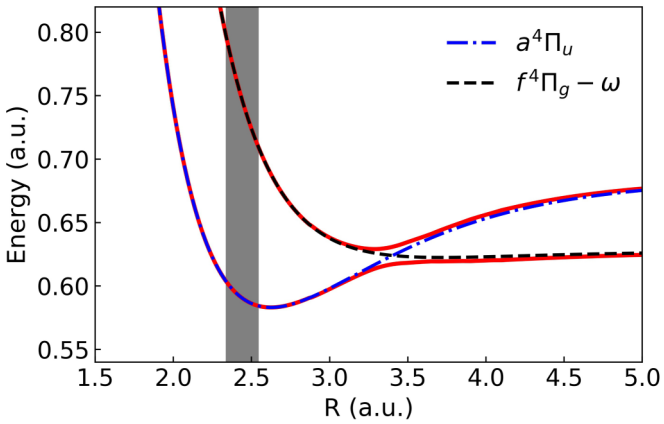

FIG. 1. Field-dressed adiabatic potential energy curves for $O_2{}^+$ for an applied external field with a wavelength of 800 nm and intensity of 10^{13} W/cm^2 (solid red curves). The corresponding field-free BO potential energy curves are shown for the cationic states, $a\,^4\Pi_u$ (dashed-dotted blue curve) and $f\,^4\Pi_g$ (dashed black curve). The shown curves correspond to cuts of the potential energy surfaces along the laser polarization direction ($\theta = 0$). The FC-transition region from the ground state of O_2 is represented by the gray vertical bar.

While several authors have investigated vibrational trapping [2,19,27–29,31–33], it is surprising that, after three decades of intense research aiming to unravel fragmentation pathways during the DI of diatomic molecules in pump-probe studies, no fully conclusive studies of pulse-intensity (or energy) dependent vibrational trapping and dissociation stabilization including rotational degrees of freedom have been published (to the best of our knowledge). For aligned $H_2{}^+$ molecular ions several theoretical studies have indicated vibrational trapping and dissociation stabilization in one-photon and three-photon bond-hardening wells [2,19,27–29,31–33]. However, the inclusion of molecular rotation was found to either eliminate three-photon trapping and reduce one-photon trapping [31] or to completely inhibit stabilization for laser parameters at which aligned-molecule calculations predict strong dissociation suppression of molecular ions that evolved out of the rotational ($J = 0$) ground state [9]. The unsettled state of intensity-depended stabilization against dissociation is in stark contrast to the well-established intensity-dependent stabilization against photoionization in intense laser fields [34,35].

More recently, noticeable progress was made in experimentally imaging and numerically modeling DI in heavier diatomic molecules, such as N_2 [14,36], O_2 [1,3,4,8,14,36], CO [14,36], and noble-gas dimers [22,37]. These investigations were carried out with IR-IR [3,14,22,36,37], XUV-IR [1,4], and XUV-XUV [8] combinations of pump and delayed probe pulses, and are being extended to IR-pump and soft x-ray probe pulse [38]. In contrast to hydrogen molecules, many-electron diatomic molecules have a complex electronic structure such that in general several adiabatic BO potential surfaces are populated during the initial ionization in the pump pulse. This makes the tracking of relevant potential surfaces in the molecular cation a challenging task that requires the scrutiny of distinct observable features in delay-dependent KER spectra. These features include fragment energies in different dissociation channels, vibrational and rotational periods and revival times in different binding potential surfaces, and electronic and vibrational level spacings. For few-photon pump or probe steps, the analysis of KER spectra can be facilitated by dipole selection rules that restrict the number of optically accessible adiabatic molecular states. The interpretation of KER spectra can be further aided by the complementary examination of fragment energies in the time and frequency domains, since the two domains tend to highlight different aspects of the nuclear dynamics [1–3,6,14].

In this work we focus on the DI of atmospherically relevant O_2 molecules. Our calculations are related to recent pump-probe experiments in which single ionization of neutral molecules in the pump pulse populates the lowest binding adiabatic states of O_2^+ [1,4,14,21]. These include the cationic ground state $O_2^+(X\ ^2\Pi_g)$, and the $a\ ^4\Pi_u$, $b\ ^4\Sigma_g$, and $f\ ^4\Pi_g$ excited states. Our theoretical analysis based on numerical nuclear wave-packet-propagation simulations indicates that the main pathway into the $O(^3P) + O^+(^4S^0)$ dissociation channel involves the launching of a nuclear wave packet by the pump pulse into the binding $O_2^+(a\ ^4\Pi_u)$ state, in which it propagates outwards (towards larger internuclear distances) and couples to the very weakly binding and predominantly repulsive $f\ ^4\Pi_g$ state. This coupling is mediated by one- or three-photon electronic transitions in the probe pulse [1,4,16]. While the coherent population and coupling of the nuclear wave packet motion in the $O_2^+(a\ ^4\Pi_u)$ and $O_2^+(f\ ^4\Pi_g)$ states explains the dominant features of the measured [1,14,21] KER spectra, very recent numerical simulations of Xue *et al.* [3] found that the addition of the binding $O_2^+(b\ ^4\Sigma_g)$ state further improves the agreement with the experimental KER spectra of De *et al.* [14] with regard to details of the measured fragment KER spectrum and its vibrational quantum-beat structure.

We here follow up on and extend our previous modeling of DI of oxygen molecules [1,2,8,14,16,36], based on the propagation of nuclear vibrational wave packets in one nuclear degree of freedom, the internuclear distance, by allowing for molecular rotation. Investigating the effects of coherent rovibrational excitation [5,9,11,12,39,40] on the dissociation dynamics of O_2^+, we assume rapid ionization of unaligned O_2 molecules, i.e., random alignment angles θ between the molecular axis and IR-laser-polarization direction, launching a rovibrational nuclear wave packet $\Psi(R,\theta,0)$ in the $O_2^+(a\ ^4\Pi_u)$ state [4]. We numerically propagate $\Psi(R,\theta,t>0)$ through a 50 fs delayed linearly polarized IR probe pulse to follow its evolution subject to IR-field-induced dipole couplings between the $O_2^+(a\ ^4\Pi_u)$ and $O_2^+(f\ ^4\Pi_g)$ states. To reveal rotational excitation and rovibrational coupling effects in O_2^+, we compare results from our rovibrational propagation calculation, treating R and θ as quantum dynamical coordinates, with propagation calculations for fixed molecular alignments (fixed θ). In our simulations for fixed alignments, we project the laser electric field on the molecular axis and treat merely R as a dynamical variable. In this paper we will refer to these simulations, allowing for or excluding rotational excitation, as "2D calculations" and "1D calculations," respectively. The analysis of our calculated O^+ fragment angular distributions and angle-integrated $O_2^+ \rightarrow O(^3P) + O^+(^4S^0)$ dissociation probabilities shows that the rotation enhances dissociation in the direction of the laser-pulse polarization. In addition, it provides evidence for transient population trapping in the light-induced vibrational bond-hardening potential well of the field-coupled $O_2^+(a\ ^4\Pi_u)$ and $O_2^+(f\ ^4\Pi_g)$ BO states to account for stabilization against dissociation for increasing pulse length (or energy). Unless stated otherwise we use atomic units throughout this work.

II. THEORETICAL METHODS

We investigate the bound and dissociative dynamics in O_2^+ molecular ions by numerically solving the TDSE within the BO approximation. We consider the vibrational and rotational dynamics restricted to the two relevant electronic states, $O_2^+(a\ ^4\Pi_u)$ and $O_2^+(f\ ^4\Pi_g)$, which we associate with the nuclear wave function components $\psi_1(R,\theta,t)$ and $\psi_2(R,\theta,t)$ of the nuclear wave packet $\Psi(R,\theta,t)$, respectively. The evolution of $\Psi(R,\theta,t)$ is thus determined by the set of coupled equations

$$i\frac{\partial}{\partial t}\begin{pmatrix}\psi_1\\ \psi_2\end{pmatrix} = \hat{H}(t)\begin{pmatrix}\psi_1\\ \psi_2\end{pmatrix}, \tag{1}$$

where the Hamiltonian for the nuclear dynamics is given by

$$\hat{H} = \begin{pmatrix} T_{\rm nuc} + V_1(R) & d_{12}(R)E(t)\cos\theta \\ d_{12}(R)E(t)\cos\theta & T_{\rm nuc} + V_2(R)\end{pmatrix}. \tag{2}$$

We adopt a coordinate system with the z axis aligned along the electric field $E(t)$ of the linearly polarized probe laser and the polar angle θ. The diagonal terms in the Hamiltonian include the nuclear kinetic energy operator $T_{\rm nuc}$ and the field-free adiabatic BO potential energy curves $V_i(R)$ of the $O_2^+(a\ ^4\Pi_u)$ $(i=1)$ and $O_2^+(f\ ^4\Pi_g)$ $(i=2)$ states (Fig. 1). The initial O_2^+ nuclear wave packet is assumed to be prepared in the $O_2^+(a\ ^4\Pi_u)$ binding electronic state via a FC transition from the ground state of the neutral O_2 molecule. Note that the transition dipole moment $d_{12}(R)$ between the $O_2^+(a\ ^4\Pi_u)$ and $O_2^+(f\ ^4\Pi_g)$ states is parallel to the molecular axis. Hence, the factor $\cos\theta$ is introduced in the off-diagonal terms to represent the interaction of the molecular ion with the laser field in dipole approximation. We calculate $V_i(R)$, $i=1,2$, and $d_{12}(R)$ using the quantum-chemistry code GAMESS (General Atomic and Molecular Electronic Structure System), as described in Ref. [16].

As mentioned in the introduction, we compare numerical calculations in which the internuclear distance R and

alignment angle θ serve as a dynamical variables (2D calculations) with simulations in which θ is a fixed parameter and rotational excitation not included (1D calculations). The corresponding nuclear kinetic energy operators are

$$T_{\rm nuc} = \frac{1}{2\mu}\begin{cases} -\frac{\partial^2}{\partial R^2} + \frac{L_\theta^2}{R^2}, & \text{2D calculation,} \\ -\frac{\partial^2}{\partial R^2}, & \text{1D calculation,} \end{cases} \tag{3}$$

with the reduced mass μ and the angular momentum operator L_θ. The comparison between these two descriptions of the nuclear dynamics provides a way to evaluate the effects of rotational excitation on the nuclear dynamics. We assume an initial rotational temperature of zero Kelvin, such that the nuclear wave packet is initialized in the rotational ground state of $O_2{}^+$ with rotational quantum number $J = 0$. Since this is an isotropic initial state propagated in a linearly polarized external field, the nuclear motion does not depend on the azimuthal angle φ.

To track rotational effects in the nuclear dynamics, we consider two laser peak intensities and different pulse durations of the probe pulse. We assume a probe-pulse electric field of the form

$$E(t) = E_0\, f(t) \sin[\omega(t - \tau_0)], \tag{4}$$

with peak amplitude E_0, a carrier frequency ω corresponding to a wavelength of 800 nm, and the field envelope

$$f(t) = \begin{cases} \cos^2\left[\frac{\pi(t-\tau_0)}{2\tau_p}\right], & \tau_0 - \tau_p \leqslant t \leqslant \tau_0 + \tau_p, \\ 0, & \text{otherwise} \end{cases} \tag{5}$$

that is centered at $\tau_0 = 50$ fs after the ionization in the pump pulse at $t = 0$. τ_p defines the probe-pulse duration as the full width at the amplitude half-maximum of $f(t)$.

Implementing the split-operator Crank-Nicolson scheme [2,41], we numerically propagate the coupled-channel TDSE (1) with time steps $\Delta t = 0.05$ a.u. on an equidistant internuclear-distance numerical grid with $N_R = 8500$ grid points and a grid spacing of $\Delta R = 0.01$ a.u. With regard to the rotational degree of freedom, we expand the nuclear wave-function components $\psi_1(t)$ and $\psi_2(t)$ in Legendre polynomials $P_J(\cos\theta)$ with $J = 0, 1, 2, \ldots, N_\theta = 79$. The expansion coefficients are determined numerically by applying a Gauss-Legendre quadrature to perform the integration over θ on a nonuniform grid [12]. To prevent unphysical reflections of the nuclear probability flux, we use a complex absorbing potential at the outermost 15 a.u. of the numerical grid. This absorber has a $\sin^2$ ramp to a maximal potential strength of magnitude 10 a.u. For the given numerical parameters all numerical results discussed in Sec. III below are converged.

From the solution of the coupled-channel equations (1) we obtain the total nuclear probability density,

$$\rho(R, \theta, t) = \sum_i |\psi_i(R, \theta, t)|^2 = \sum_i \rho_i(R, \theta, t), \tag{6}$$

in terms of the partial densities $\rho_i(R, \theta, t)$, $i = 1, 2$, associated with the $O_2{}^+(a\ {}^4\Pi_u)$ and $O_2{}^+(f\ {}^4\Pi_g)$ channels. We calculate the angular distribution of photofragments according to

$$P(\theta) = \int_{R_1}^{R_{\rm max}} dR\, \rho(R, \theta, t = T), \tag{7}$$

where $R_{\rm max} = 85$ a.u. is the radial extent of the numerical grid. In our numerical applications in Sec. III, we find a propagation time of $T = 800$ fs to be sufficiently long to yield converged angular distributions $P(\theta)$. During the propagation of the $O_2{}^+$ nuclear wave packet, bound and dissociative components of the evolving nuclear probability density can be distinguished [2,16]. For the numerical applications discussed below, we find that the bound nuclear motion is limited to internuclear distances smaller than $R_1 = 6$ a.u. and exclude this effective range in Eq. (7).

Aside from assessing the influence of rotational excitation on fragment angular distributions, we also explore molecular-bond stabilization during the propagation of the nuclear wave packet in the probe-laser field. For this purpose, we calculate the total, angle-integrated dissociation probabilities

$$P_{\rm tot} = \int_0^\pi d\theta\, \sin\theta P(\theta). \tag{8}$$

As an additional tool for examining the nuclear dynamics and identifying population trapping in light-induced potential wells, we Fourier transform the numerically calculated partial nuclear probability densities $\rho_i(R, \theta, t)$ (Sec. III C). This type of quantum-beat analysis has been shown to be capable of revealing the nodal structure of pairs of beating rovibrational states, the spatial extent of the bound nuclear motion, bond softening and hardening, as well as the outline of field-dressed adiabatic molecular potential curves [2,6,11,12,19].

III. RESULTS AND DISCUSSION

A. Angular distributions of photofragments

In this section we analyze the results from our coupled-channel TDSE calculations for the strong-field dissociation dynamics in $O_2{}^+$. Assessing the role of rotational excitation, we compare numerical results from 2D calculations with corresponding 1D calculations at fixed molecular alignment angle θ. First, we discuss the case where the nuclear wave packet is initialized from an isotropic distribution of randomly aligned $O_2{}^+$ molecular ions and then exposed to an 800 nm probe pulse with a delay of $\tau_0 = 50$ fs. In Sec. III C we examine the rovibrational dynamics in an 800 nm continuum-wave driving field.

Figure 2 shows calculated angular distributions of photofragments $P(\theta)$ according to Eq. (7) for two laser peak intensities, 3×10^{14} W/cm^2 (upper panels) and 6×10^{14} W/cm^2 (lower panels). In addition to the dependence on the laser intensity, individual panels in Fig. 2 display the variation of $P(\theta)$ with the duration τ_p of the probe-pulse field. Angular distributions from 1D and 2D calculations are indicated by the dashed red and solid blue curves, respectively. Since the transition-dipole moment $d_{12}(R)$ is parallel to the molecular axis, $O_2{}^+$ molecular ions that are initially aligned at a given angle θ experience an effective peak intensity $I_{\rm eff} = I_0 \cos^2\theta$, where $I_0 \sim E_0^2$ is the laser peak intensity. Based on this expression, we expect fragmentation for molecular ions aligned along the laser polarization (i.e., for $\theta = 0$) to be most prominent. Indeed, for most pulse durations, both intensities, and according to both 1D and 2D calculations, Fig. 2 demonstrates that dissociation preferentially occurs for $\theta = 0$. Notably, we find an overall enhancement of the $O_2{}^+$

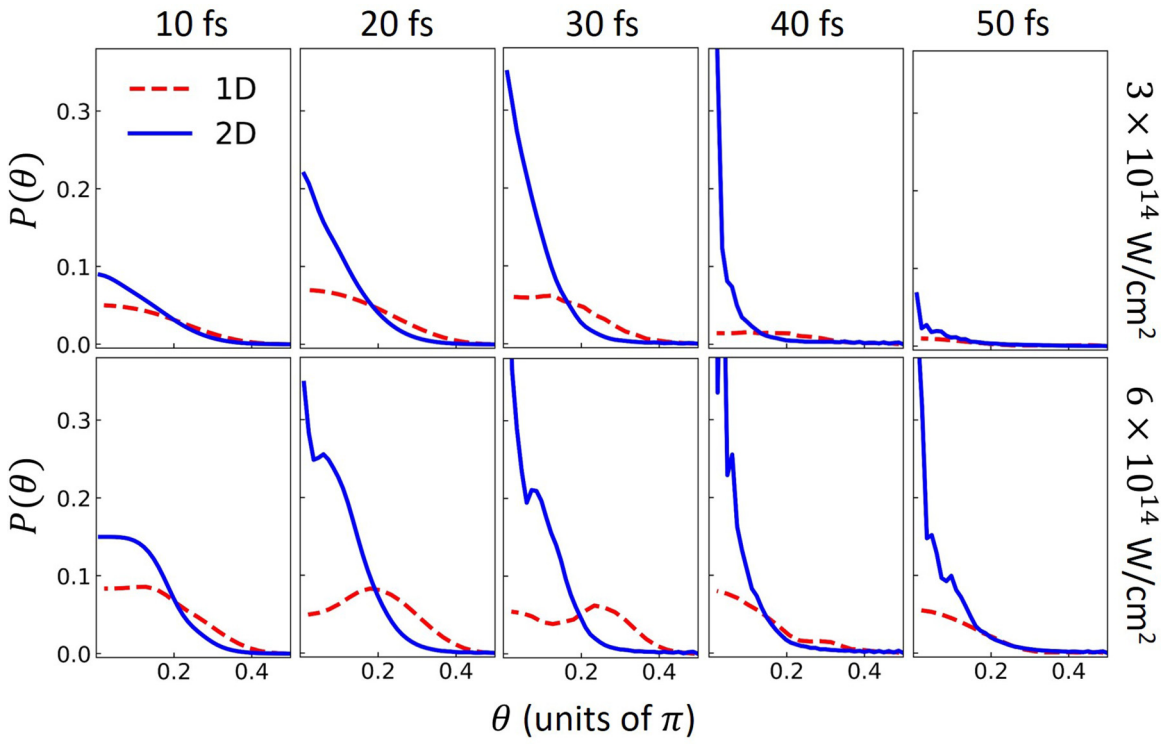

FIG. 2. Angular distribution of O^+ fragments for 50 fs delayed 800 nm probe laser pulses with peak intensities of 3×10^{14} W/cm^2 (upper panels) and 6×10^{14} W/cm^2 (lower panels) and pulse durations between 10 and 50 fs (from left to right). Dashed red and solid blue curves are results for calculations without (1D) and including rotational excitation (2D), respectively.

dissociation yield in the 2D results close to $\theta = 0$, when compared to the 1D results. For both laser intensities, the 2D model predicts a more drastic dissociation enhancement close to $\theta = 0$ for increasing pulse length (i.e., pulse energy) than the 1D model.

Based on resonant single-photon transitions dominating the coupling to the dissociating $O_2^+(f\ ^4\Pi_g)$ state, one might expect a $\cos^2\theta$ shaped fragment angular distribution. As seen in Fig. 2, the angular distributions obtained from the 2D model more or less approximately follow this functional form, strongly depending on laser peak intensity and pulse duration. For both laser intensities, Fig. 2 demonstrates that the corresponding angular distributions from the 2D model become narrower as the pulse duration is increased. These narrower distributions can be matched by including higher powers of $\cos\theta$ in $P(\theta)$ and thus, in general, point to rotational excitation [42–44]. The comparison of 1D and 2D results in Fig. 2 reveals that deviations from the $\cos^2\theta$ dependence are primarily due to rotational excitation. Specifically, the differences between the 1D and 2D angular distributions signify the *dynamical alignment* of the O_2^+ molecular ions along the polarization direction of the probe-laser field. In other words, a fraction of the initially unaligned molecular ions become preferentially aligned along the laser polarization direction [45]. Our results thus emphasize the importance of rotational excitations in calculating $P(\theta)$, even for the shortest pulse duration that we have considered, 10 fs. This is consistent with previous theoretical and experimental studies of the dissociative dynamics of H_2 and O_2 molecules and their respective molecular cations [9,10,39,44,46].

As discussed above, we find that dynamical alignment becomes more important for increasing pulse duration. Generally speaking, the role of dynamical alignment is expected to be more significant for relatively long pulse durations since there is more time for rotational excitation. Based on this scenario, a longer pulse duration τ_p would provide a higher degree of preferential alignment in the O_2^+ molecular ions, which in turn would tend to enhance the total dissociation yield. Interestingly, our calculations reveal that increasing the pulse duration does not necessarily result in the overall enhancement of the dissociation yield. For instance, for a 50 fs laser pulse with a peak intensity of 3×10^{14} W/cm^2, the angular distributions from both the 1D and 2D models exhibit lower dissociation yields compared to shorter laser pulses with the same intensity (Fig. 2). This suppression of the dissociation yield with respect to increasing pulse duration is a possible signature of (light-induced) bond hardening. In the next subsections, we will further examine the underlying mechanism behind this molecular stabilization effect.

Aside from the effects associated with dynamical alignment, we also note that some of the 2D angular distributions in Fig. 2 have distinct modulations. These are the most pronounced at the higher shown laser intensity and for pulse durations of 20 fs and longer. Within the Floquet description of the molecular strong-field dynamics, we provide two possible explanations for the occurrence of these modulations. First, these modulations can be understood in terms of light-induced conical intersections (LICIs) between different potential energy surfaces [5,47,48]. Indeed, interference effects in the

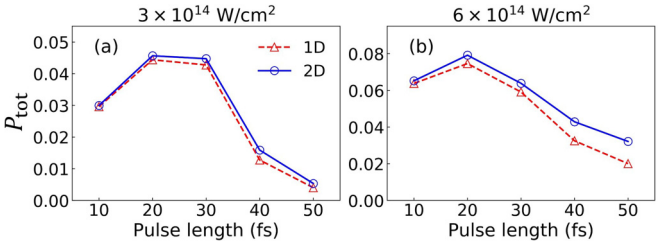

FIG. 3. Total, angle-integrated dissociation probabilities P_{tot} of O_2^+ molecular ions as functions of the pulse duration for the same laser parameters as in Fig. 2, (a) 3×10^{14} W/cm^2 and (b) 6×10^{14} W/cm^2. Red triangles and blue circles are results from calculations without (1D) and including rotational excitation (2D), respectively, interpolated by straight lines to guide the eye.

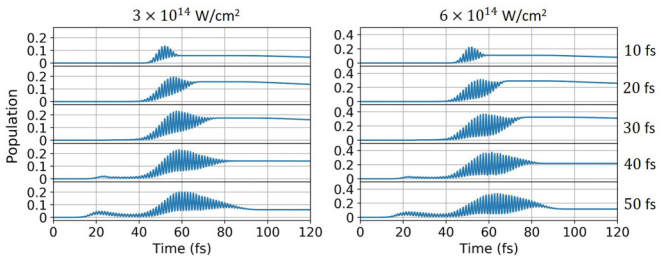

FIG. 4. Transient population transfer to the $O_2^+(f\ ^4\Pi_g)$ channel during the probe-field-coupled nuclear motion in the $O_2^+(a\ ^4\Pi_u)$ and $O_2^+(f\ ^4\Pi_g)$ BO states for 50 fs delayed 800 nm cos^2 probe pulses with peak intensities of 3×10^{14} W/cm^2 (left panel) and 6×10^{14} W/cm^2 (right panel). In each panel the probe-pulse lengths increases from 10 fs (top) to 50 fs (bottom). The population transfers are calculated for binding internuclear distances $R \leqslant 6$ a.u.

nuclear wave-packet dynamics near LICIs have been shown theoretically to yield modulations in the fragment angular distributions for the strong-field-induced dissociation of D_2^+ [49,50] and have recently been confirmed experimentally in energy- and angle-resolved fragment distributions for the dissociation of H_2^+ in intense IR pulses [48]. In our two-state 2D calculations, the LICI is located at the crossing of the field-dressed $O_2^+(a\ ^4\Pi_u)$ and $O_2^+(f\ ^4\Pi_g)$ potential surfaces at the polar angle $\theta = \pi/2$ and the internuclear distance where $V_1(R) = V_2(R) - \omega$. We thus tentatively attribute some of the sharp angular modulations in Fig. 2 to the same interference mechanism that was revealed in Refs. [48–50] for hydrogen molecular cations.

The second explanation for the presence of modulations in the angular distributions is bond hardening. Since the 1D model does not include LICIs, the modulations in the 1D results cannot be related to a LICI. For instance, for 6×10^{14} W/cm^2 20 fs probe pulses, the 1D model predicts suppressed dissociation for aligned molecular ions. We note that modulations in fragment angular distributions were recently also found in two- and three-state 1D and 2D numerical simulations of the light-induced photodissociation of LiF molecules [5]. In agreement with our findings, these calculations for polar molecules demonstrate that bond-hardening above LICIs can suppress dissociation along the direction of the transition dipole moment.

B. Molecular bond stabilization

Next, we analyze the bond hardening mechanism and associated molecular stabilization effects [2,19,28,29] in the dissociation of O_2^+. The left and right panels of Fig. 3 show the angle-integrated dissociation probability P_{tot} according to Eq. (8) as a function of the laser pulse duration for the same peak intensities, 3×10^{14} W/cm^2 [Fig. 3(a)] and 6×10^{14} W/cm^2 [Fig. 3(b)], as Fig. 2. Since a longer pulse allows more time for population transfer to the dissociating $O_2^+(f\ ^4\Pi_g)$ state, one might intuitively expect P_{tot} to increase monotonically with the pulse duration. However, as seen in Fig. 3 for both considered pulse intensities, the calculated total dissociation probabilities begin to decrease for laser-pulse durations above 20 fs. This decrease is observed in both 1D and 2D calculations. Dissociation stabilization thus persists when molecular rotation is included.

For the considered pulse lengths, our 2D calculations predict larger fragment yields than the 1D model. This is consistent with an effective centrifugal force promoting fragmentation [51]. However, the inclusion of molecular rotation in the present case only results in a very small increase of P_{tot} at a peak intensity of 3×10^{14} W/cm^2 [Fig. 3(a)] and does not qualitatively change the pulse-length dependence at either intensity in Fig. 3. We attribute the deviation between the 1D and 2D yields in Fig. 3(b), particularly for the longer pulse durations, to dissociation enhancement due to dynamical alignment. However, this alignment is not strong enough to counteract the pulse-length-dependent stabilization. Our numerical simulations confirm that this pulse-length (energy) dependent stabilization persists at even lower peak intensities of $\sim 10^{13}$ W/cm^2.

Bond hardening can also be quantified by following the evolution of the population transfer to the $O_2^+(f\ ^4\Pi_g)$ channel as given by the partial nuclear probability density $\rho_2(R, \theta, t)$ in Eq. (6). The graphs in Fig. 4 show the transient population

$$P[f\ ^4\Pi_g](t) = \int_0^{R_1} dR \int_0^{\pi} d\theta \sin\theta\, \rho_2(R, \theta, t) \qquad (9)$$

for the same 800 nm cos^2 probe pulses with the same peak intensities and pulse lengths as in Figs. 2 and 3. The rapid population oscillations correspond to laser-driven Rabi flops between the $O_2^+(a\ ^4\Pi_u)$ and $O_2^+(f\ ^4\Pi_g)$ states. For pulse durations below 30 fs, these transitions occur due to the absorption and emission of a single IR photon, while for pulse lengths of 40 and 50 fs the envelope of the $O_2^+(f\ ^4\Pi_g)$-channel population shows two maxima that correspond to three-photon followed by single-photon transitions. Consistent with the pulse-length-dependent dissociation stabilization exposed in Fig. 3, the $O_2^+(f\ ^4\Pi_g)$-channel population after the end of the probe pulse is a nonmonotonic function of the pulse length and largest at a pulse length of 30 fs (Fig. 4). Comparing the left and right panels of Fig. 4, we find overall very similar patterns in population transfer for both pulse intensities.

We note that the final populations in Fig. 4 do not directly correspond to the total dissociation yields in Fig. 3, since

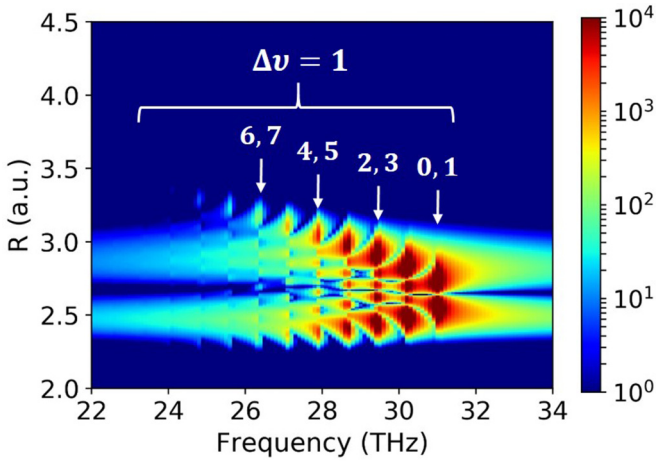

FIG. 5. Vibrational quantum-beat spectrum for the field-free evolution of the nuclear probability density in the binding $O_2^+(a\ ^4\Pi_u)$ BO state. Selected pairs of beating vibrational states are indicated by short white arrows and corresponding vibrational quantum numbers.

some population remains trapped in the shallow well of the field-free $O_2^+(f\ ^4\Pi_g)$ state after the probe pulse has faded away. Nevertheless, the transient trapping of population in the upper light-dressed state plays an important role in the dissociation process, especially for sufficiently long pulse durations.

C. Quantum-beat analysis

To further examine the effects of rotational excitation on $P(\theta)$ and on bond stabilization in the angle-integrated dissociation probability $P_{\rm tot}$ shown in Figs. 2 and 3, respectively, we investigate the coherent nuclear wave-packet evolution in the frequency domain. For details of the calculation and properties of vibrational and rotational quantum-beat spectra see Refs. [6,11,12]. Rather than examining fully differential quantum-beat spectra as a function of the rotational and vibrational degrees of freedom, for the present study we found it more conclusive to average over the rotational motion as detailed in Eq. (21) of Ref. [12]. In order to more clearly illustrate the effects of the light-induced coupling between the $O_2^+(a\ ^4\Pi_u)$ and $O_2^+(f\ ^4\Pi_g)$ potential surfaces, we scrutinize the nuclear motion for a total propagation time of 10 ps subject to a 10^{14} W/cm^2 flat-top probe field with a $\sin^2$ ramp, starting at $t = 0$, and a ramp-up time of 50 fs.

As a reference, Fig. 5 shows the vibrational quantum-beat spectrum for the free evolution of the FC wave-packet created by the assumed instantaneous ionization in the pump pulse. The field-free spectrum clearly displays quantum beats between adjacent vibrational states in the $O_2^+(a\ ^4\Pi_u)$ electronic state. These are indicated by white arrows and labeled with the vibrational quantum numbers ν of the beating states. Along the internuclear-distance axis, each quantum-beat line displays the nodal structures of the two beating states and the product of their probability densities.

The quantum-beat spectra in Fig. 6 are obtained by Fourier transformation of the partial nuclear probability densities $\rho_i(R,\theta,t)$, $i = 1, 2$, associated with the $O_2^+(a\ ^4\Pi_u)$ and $O_2^+(f\ ^4\Pi_g)$ BO electronic states. The Fourier transformation is windowed over the 10 ps delay range that allows the resolution of vibrational and rotational quantum-beat frequencies [6,11,12]. Vertical quantum-beat lines in all panels of Fig. 6 correspond to beating vibrational states.

The comparison of the field-free spectrum in Fig. 5 and the field-dressed spectrum in Fig. 6(a) reveals a strong influence of the external field. Due to the external electric field of the probe pulse, the beat frequencies in Fig. 6(a) are redshifted relative to the corresponding quantum beats in Fig. 5. This redshift is consistent with the field-induced widening of the $O_2^+(a\ ^4\Pi_u)$ well (Fig. 1). Corresponding beat frequencies in Figs. 5 and 6(a) are easily recognized by identical numbers of nodes along the R axis [6,15]. While the field-free spectrum (Fig. 5) only reveals quantum beats between adjacent vibrational states (with the difference of vibrational quantum numbers $\Delta\nu = 1$), the field-dressed spectra in Fig. 6 also include fainter "intruder lines" from overtones (with $\Delta\nu > 1$). Some intruder lines are circled in Fig. 6(a) and cannot be assigned to corresponding quantum beats in Fig. 5.

Figures 6(a) and 6(b) show quantum-beat spectra for molecular ions according to our 1D model, not allowing for rotational excitation and assuming the cations remain aligned along the probe-laser polarization ($\theta = 0$). The beat frequencies in the field-dressed $O_2^+(a\ ^4\Pi_u)$ [Fig. 6(a)] and $O_2^+(f\ ^4\Pi_g)$ channels [Fig. 6(b)] coincide.

The weak signal strength in the $O_2^+(f\ ^4\Pi_g)$ channel [Figs. 6(b)–6(d)] indicates the portion of the nuclear wave packet that is transiently trapped in the light-dressed $O_2^+(f\ ^4\Pi_g)$ state. This population trapping is related to the suppressed dissociation shown for pulse lengths of 20 fs and longer in Fig. 3. It is akin to IR-pulse-induced bond hardening and molecular stabilization, predicted almost three decades ago for vibrationally excited H_2^+ molecular ions in time-independent Floquet wave-packet-propagation calculations [28]. This bond hardening is consistent with the results of our 2D calculations in Fig. 4, showing a decrease in the final population transferred to the field-dressed $O_2^+(f\ ^4\Pi_g)$ state for pulse durations longer than 30 fs. It suggests that the dissociation stabilization shown in Fig. 3 profits from the external field more effectively driving nuclear probability density back down to the binding $O_2^+(a\ ^4\Pi_u)$ state as the pulse length increases. The comparison of Fig. 6(b) with Figs. 6(c) and 6(d) indicates that this interdependence of bond hardening and pulse-dependent dissociation stabilization persists when molecular rotation is included with regard to both the incoherent average over initial alignments of the molecular cation [Fig. 6(c)] and rotational excitation [Fig. 6(d)]. The many additional lines seen in Figs. 6(c) and 6(d) are due to the variation of the quantum-beat frequencies with the alignment-angle-dependent effective (projected) laser intensity. Additional lines in Fig. 6(d) are also related to rotational quantum-beat lines [11,12].

IV. SUMMARY AND CONCLUSIONS

We analyzed the coherent rovibrational nuclear motion in O_2^+ molecular ions out of an initial FC wave packet in the $O_2^+(a\ ^4\Pi_u)$ BO state, subject to light-induced coupling to the weakly binding, primarily repulsive $O_2^+(f\ ^4\Pi_g)$

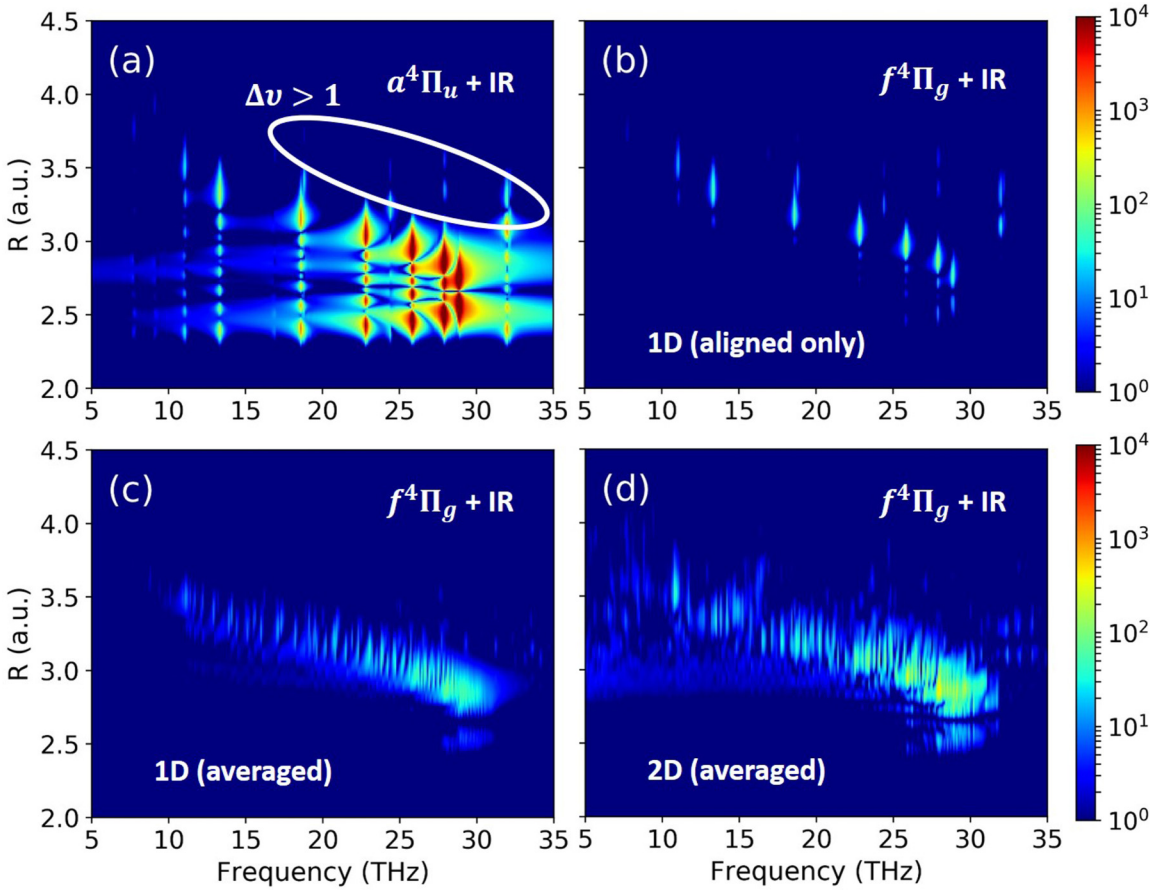

FIG. 6. Quantum-beat spectra for the nuclear motion in the $O_2^+(a\ ^4\Pi_u)$ and $O_2^+(f\ ^4\Pi_g)$ BO electronic states coupled by a 800 nm 10^{14} W/cm^2 continuous wave laser electric field with a leading 50 fs $\sin^2$ ramp. The quantum-beat analysis is applied to the components ρ_1 and ρ_2 of the nuclear probability density in the $O_2^+(a\ ^4\Pi_u)$ and $O_2^+(f\ ^4\Pi_g)$ channels [cf. Eqs. (1) and (6)]. Upper panels: Field-induced motion along the laser-polarization direction without rotational excitation according to 1D calculations. (a) $O_2^+(a\ ^4\Pi_u)$ channel. Some of the faint intruder quantum-beat lines are indicated in the white oval. (b) $O_2^+(f\ ^4\Pi_g)$ channel. Lower panels: Field-induced motion in the $O_2^+(f\ ^4\Pi_g)$ channel. (c) 1D calculations performed for fixed alignment angles θ averaged over θ. (d) 2D calculations allowing for rotational excitation for the propagation of an initial $J = 0$ $O_2^+(f\ ^4\Pi_g)$ FC wave packet averaged over θ.

state. Our analysis uncovers the importance of the bond-hardening mechanism in O_2^+ and reveals its signature as a bond stabilization effect for sufficiently long probe-pulse durations. Specifically, for an initial distribution of randomly aligned molecular ions and fixed peak intensities, our numerical results show transient population trapping in the bond-hardening well of the field-dressed $O_2^+(a\ ^4\Pi_u)$ and $O_2^+(f\ ^4\Pi_g)$ states and stabilization of $O_2^+ \rightarrow O(^3P) + O^+(^4S^0)$ dissociation as the length of the probe pulse exceeds 20 fs. By examining the evolution of the population transfer to the $O_2^+(f\ ^4\Pi_g)$ channel in the time and quantum-beat frequency domains, we find this pulse-length-dependent dissociation stabilization to be consistent with transient population trapping in the light-dressed $O_2^+(f\ ^4\Pi_g)$ state that results from the one- and three-photon couplings of the field-free $a\ ^4\Pi_u$ and $f\ ^4\Pi_g$ BO states of O_2^+.

While our numerical model provides strong evidence for the observable occurrence of probe-pulse-duration-dependent dissociation stabilization in O_2^+ due to bond hardening, there is no "one-size-fits-all" answer to how exactly, where, and when molecular-bond stabilization occurs and the effect it has in measured dissociation yields and KER spectra. This calls for further studies with (a) an extended range of laser parameters, (b) different initial rovibrational distributions of molecular cations, and (c) other small molecules.

ACKNOWLEDGMENTS

We thank Christine Aikens, Itzik Ben-Itzhak, Vinod Kumarappan, and Artem Rudenko for fruitful discussions. This work was supported by the Chemical Sciences, Geosciences, and Biosciences Division, Office of Basic Energy Sciences, Office of Science, U.S. Department of Energy under Award No. DEFG02-86ER13491. For part of the code development and for computational hardware we acknowledge support by NSF Grant No. PHY 1802085. We also acknowledge access to the Beocat Research Cluster at Kansas State University.

[1] P. Cörlin, A. Fischer, M. Schönwald, A. Sperl, T. Mizuno, U. Thumm, T. Pfeifer, and R. Moshammer, Phys. Rev. A **91**, 043415 (2015).

[2] M. Magrakvelidze, A. Kramer, K. Bartschat, and U. Thumm, J. Phys. B **47**, 124003 (2014).

[3] S. Xue, H. Du, B. Hu, C. D. Lin, and A.-T. Le, Phys. Rev. A **97**, 043409 (2018).

[4] Y. Malakar, F. Wilhelm, D. Trabert, Kanaka Raju P., X. Li, W. L. Pearson, W. Cao, B. Kaderiya, I. Ben-Itzhak, and A. Rudenko, Phys. Rev. A **98**, 013418 (2018).

[5] A. Tóth, A. Csehi, G. J. Halász, and A. Vibók, Phys. Rev. A **99**, 043424 (2019).

[6] U. Thumm, T. Niederhausen, and B. Feuerstein, Phys. Rev. A **77**, 063401 (2008).

[7] T. Ergler, A. Rudenko, B. Feuerstein, K. Zrost, C. D. Schröter, R. Moshammer, and J. Ullrich, Phys. Rev. Lett. **97**, 193001 (2006).

[8] M. Magrakvelidze, O. Herrwerth, Y. H. Jiang, A. Rudenko, M. Kurka, L. Foucar, K. U. Kühnel, M. Kübel, N. G. Johnson, C. D. Schröter, S. Düsterer, R. Treusch, M. Lezius, I. Ben-Itzhak, R. Moshammer, J. Ullrich, M. F. Kling, and U. Thumm, Phys. Rev. A **86**, 013415 (2012).

[9] F. Anis and B. D. Esry, Phys. Rev. A **77**, 033416 (2008).

[10] F. Anis, T. Cackowski, and B. D. Esry, J. Phys. B **42**, 091001 (2009).

[11] M. Winter, R. Schmidt, and U. Thumm, Phys. Rev. A **80**, 031401(R) (2009).

[12] M. Winter, R. Schmidt, and U. Thumm, New J. Phys. **12**, 023020 (2010).

[13] R. Robinett, Phys. Rep. **392**, 1 (2004).

[14] S. De, M. Magrakvelidze, I. A. Bocharova, D. Ray, W. Cao, I. Znakovskaya, H. Li, Z. Wang, G. Laurent, U. Thumm, M. F. Kling, I. V. Litvinyuk, I. Ben-Itzhak, and C. L. Cocke, Phys. Rev. A **84**, 043410 (2011).

[15] B. Feuerstein, T. Ergler, A. Rudenko, K. Zrost, C. D. Schröter, R. Moshammer, J. Ullrich, T. Niederhausen, and U. Thumm, Phys. Rev. Lett. **99**, 153002 (2007).

[16] M. Magrakvelidze, C. M. Aikens, and U. Thumm, Phys. Rev. A **86**, 023402 (2012).

[17] A. Zewail, Science **242**, 1645 (1988).

[18] A. S. Alnaser, B. Ulrich, X. M. Tong, I. V. Litvinyuk, C. M. Maharjan, P. Ranitovic, T. Osipov, R. Ali, S. Ghimire, Z. Chang, C. D. Lin, and C. L. Cocke, Phys. Rev. A **72**, 030702(R) (2005).

[19] M. Magrakvelidze, F. He, T. Niederhausen, I. V. Litvinyuk, and U. Thumm, Phys. Rev. A **79**, 033410 (2009).

[20] A. Zewail, J. Phys. Chem. A **104**, 5660 (2000).

[21] S. De, I. A. Bocharova, M. Magrakvelidze, D. Ray, W. Cao, B. Bergues, U. Thumm, M. F. Kling, I. V. Litvinyuk, and C. L. Cocke, Phys. Rev. A **82**, 013408 (2010).

[22] J. Wu, M. Magrakvelidze, A. Vredenborg, L. P. H. Schmidt, T. Jahnke, A. Czasch, R. Dörner, and U. Thumm, Phys. Rev. Lett. **110**, 033005 (2013).

[23] H. Ibrahim, C. Lefebvre, A. D. Bandrauk, A. Staudte, and F. Légaré, J. Phys. B: At. Mol. Opt. Phys. **51**, 042002 (2018).

[24] T. Seideman, M. Y. Ivanov, and P. B. Corkum, Phys. Rev. Lett. **75**, 2819 (1995).

[25] S. Chelkowski, A. Conjusteau, T. Zou, and A. D. Bandrauk, Phys. Rev. A **54**, 3235 (1996).

[26] B. Feuerstein and U. Thumm, Phys. Rev. A **67**, 063408 (2003).

[27] P. H. Bucksbaum, A. Zavriyev, H. G. Muller, and D. W. Schumacher, Phys. Rev. Lett. **64**, 1883 (1990).

[28] G. Yao and S.-I. Chu, Phys. Rev. A **48**, 485 (1993).

[29] L. J. Frasinski, J. H. Posthumus, J. Plumridge, K. Codling, P. F. Taday, and A. J. Langley, Phys. Rev. Lett. **83**, 3625 (1999).

[30] S. R. Barone, M. A. Narcowich, and F. J. Narcowich, Phys. Rev. A **15**, 1109 (1977).

[31] E. E. Aubanel, A. Conjusteau, and A. D. Bandrauk, Phys. Rev. A **48**, R4011 (1993).

[32] E. E. Aubanel, J.-M. Gauthier, and A. D. Bandrauk, Phys. Rev. A **48**, 2145 (1993).

[33] A. Giusti-Suzor, F. H. Mies, L. F. DiMauro, E. Charron, and B. Yang, J. Phys. B **28**, 309 (1995).

[34] M. Protopapas, C. H. Keitel, and P. L. Knight, Rep. Prog. Phys. **60**, 389 (1997).

[35] A. M. Popov, O. V. Tikhonova, and E. A. Volkova, J. Phys. B **36**, R125 (2003).

[36] I. A. Bocharova, A. S. Alnaser, U. Thumm, T. Niederhausen, D. Ray, C. L. Cocke, and I. V. Litvinyuk, Phys. Rev. A **83**, 013417 (2011).

[37] M. Magrakvelidze and U. Thumm, Phys. Rev. A **88**, 013413 (2013).

[38] N. Saito, H. Sannohe, N. Ishii, T. Kanai, N. Kosugi, Y. Wu, A. Chew, S. Han, Z. Chang, and J. Itatani, Optica **6**, 1542 (2019).

[39] X. M. Tong, Z. X. Zhao, A. S. Alnaser, S. Voss, C. L. Cocke, and C. D. Lin, J. Phys. B **38**, 333 (2005).

[40] Y. Yu, S. Zeng, J. V. Hernández, Y. Wang, and B. D. Esry, Phys. Rev. A **94**, 023423 (2016).

[41] M. R. Hermann and J. A. Fleck, Phys. Rev. A **38**, 6000 (1988).

[42] M. R. Thompson, M. K. Thomas, P. F. Taday, J. H. Posthumus, A. J. Langley, L. J. Frasinski, and K. Codling, J. Phys. B **30**, 5755 (1997).

[43] K. Sändig, H. Figger, and T. W. Hänsch, Phys. Rev. Lett. **85**, 4876 (2000).

[44] J. McKenna, F. Anis, A. M. Sayler, B. Gaire, N. G. Johnson, E. Parke, K. D. Carnes, B. D. Esry, and I. Ben-Itzhak, Phys. Rev. A **85**, 023405 (2012).

[45] J. H. Posthumus, J. Plumridge, M. K. Thomas, K. Codling, L. J. Frasinski, A. J. Langley, and P. F. Taday, J. Phys. B **31**, L553 (1998).

[46] J. McKenna, A. M. Sayler, F. Anis, B. Gaire, N. G. Johnson, E. Parke, J. J. Hua, H. Mashiko, C. M. Nakamura, E. Moon, Z. Chang, K. D. Carnes, B. D. Esry, and I. Ben-Itzhak, Phys. Rev. Lett. **100**, 133001 (2008).

[47] N. Moiseyev, M. Šindelka, and L. S. Cederbaum, J. Phys. B **41**, 221001 (2008).

[48] A. Natan, M. R. Ware, V. S. Prabhudesai, U. Lev, B. D. Bruner, O. Heber, and P. H. Bucksbaum, Phys. Rev. Lett. **116**, 143004 (2016).

[49] G. J. Halász, Á. Vibók, N. Moiseyev, and L. S. Cederbaum, Phys. Rev. A **88**, 043413 (2013).

[50] G. J. Halász, Á. Vibók, and L. S. Cederbaum, J. Phys. Chem. Lett. **6**, 348 (2015).

[51] M. Fischer, U. Lorenz, B. Schmidt, and R. Schmidt, Phys. Rev. A **84**, 033422 (2011).